SCITECH Forum, 54th AIAA Aerospace Sciences Meeting, 4-8 January 2016, San Diego, California, USA
Paper number AIAA 2016-0764
https://doi.org/10.2514/6.2016-0764

Aerodynamics of aero-engine installation

Tomasz P. Stańkowski[1], David G. MacManus[2]
Cranfield University, Bedford, United Kingdom, MK43 0AL

Christopher T. Sheaf[3], Nicholas Grech[4]
Rolls-Royce plc, P.O Box 31
Derby, United Kingdom, DE24 8BJ

Nomenclature

b	=	wing span
c	=	aircraft reference chord
c_{loc}	=	aircraft local chord
dc	=	aircraft drag counts, based on aircraft reference area
C_D	=	drag coefficient based on aircraft reference area
C_d	=	discharge coefficient
C_f	=	skin friction coefficient
C_p	=	pressure coefficient
C_L	=	lift coefficient
D_{FF}	=	fan face diameter
D_{max}	=	nacelle maximum diameter
D	=	drag force
L	=	lift force
L_{nac}	=	length of a nacelle
M	=	Mach number
V	=	Velocity
x,y,z	=	Cartesian coordinate system for the aircraft
ξ, η, ζ	=	Cartesian coordinate system for the engine
ξ, R, Θ	=	Cylindrical coordinate system for the engine
ϕ	=	force in the drag domain
θ	=	force in the thrust domain

Acronyms

AoA	=	Angle of Attack
AoA_{eng}	=	Effective angle of attack for an engine
$AoA_{A/c}$	=	Angle of attack for an aircraft axis
AoA_{inst}	=	Geometrical angle of engine installation
CRM	=	NASA Common Research Model
GPF	=	Gross Propulsive Force
MFCR	=	mass flow capture ratio
NPF	=	Net Propulsive Force
NPR	=	Nozzle Pressure Ratio
TET	=	Turbine Entry Temperature
TFN	=	Through Flow Nacelle
WB	=	Wing Body
WBNP	=	Wing Body with Nacelle and Pylon
WBT0	=	Wing Body with 0° inclined Tailplane
WBT0NP	=	Wing Body Tail with Nacelle and Pylon

[1]PhD Student Researcher, Propulsion Engineering Centre, Cranfield University
[2]Head of Gas Turbine Technology Group, Propulsion Engineering Centre, Cranfield University
[3]Installations Aerodynamics specialist
[4]Aerothermal Engineer – Installations Aerodynamics

I. Introduction

To meet the expected future improvements in overall aircraft efficiency, it is necessary to ensure that the installation and integration of the engine with the airframe is properly assessed. The increased interest of the aerodynamic interference in the context of turbofan integration[1] appeared around the early 1980s mainly as a result of the increased diameter of turbofan engines. Moreover, a range of experimental studies was dedicated to the problem of podded nacelle installation under a swept transonic wing of a typical transport aircraft[2, 3]. The studies indicated that the installation drag for two nacelles in the order of 75 dc. The key parameters that affect the installation drag were defined as nacelle axial and vertical position and nacelle toe-in angle. Currently, the effect of engine installation for a typical conventional podded under-wing engine for a wide-body twin-engine aircraft is estimated to be in the order of 30 to 50 drag counts per two engines[4], although it is sensitive to the relative engine size and position on the wing[4, 5, 6]. The effect of engine size becomes significant for larger diameters[7]. Due to the large number of degrees of freedom, computational methods such as Euler evaluations were considered to analyse the multitude of potential configurations[8]. Furthermore, the development of numerical tools and an increase in computational power led a series of Drag Prediction Workshops, where the second workshop was dedicated to installation effects[9]. The success of the initial workshop triggered the design of more a modern geometry for the NASA Common Research Model[10]. The publication of substantial experimental datasets with and without through-flow nacelles[11, 12] makes the Common Research Model (CRM) a benchmark validation activity to assess the effects of installation. Within this broad context, it is anticipated that engine installation will become an increasingly important concern as engine diameters are expected to increase in pursuit of improved propulsive efficiency. It is also expected that knowledge of these aspects at the preliminary design stage will become more important to facilitate timely and informed decisions on engine cycle, size and airframe integration. A key element of the development of future civil aircraft is a robust assessment of the mutual interactions, and therefore of the thrust and drag characteristics, of the combined engine and aircraft configuration. The aim of this research is to study the details of aerodynamics for aero-engine installation. The long-term purpose is to create a framework that will evaluate the combined engine and aircraft configuration for a specified flight mission and that could be applied at a preliminary design stage. In this context, the current paper presents the drag assessments for engine installation, where the work was carried out with use of the NASA CRM modified to include an under-wing turbofan engine with a separate-jet exhaust system. The paper concentrates on the flow physics that define the aerodynamic interference and characteristics for aero-engine installations.

II. Methods and scope

A key focus of the current work is the use of computational fluid dynamics (CFD) to evaluate the installation aerodynamic effects for podded underwing engine configurations. The current research provides an in-depth understanding of key sensitivities in engine under-wing installations. The installation effects are assessed for sensitivities to aircraft incidence and engine positions. This work aims to explain the flow physics, as well as, to identify and to quantify the aerodynamic mechanisms that govern engine installation effects both in the drag and thrust domain.

A. Project scope

The overall project scope is to assess the impact of installation effects at cruise conditions, as it is the dominant phase for long-haul flights. A typical mission at altitude of 35000 ft, cruise Mach number of 0.82 and aircraft angles of attack between 0° and 5° was chosen for the NASA CRM[10], which is a civil transport configuration broadly similar to a typical wide body aircraft with 250-300 passenger seats. A range of engine positions (Table 1) was considered based on the position of the fan cowl trailing edge in relation to the wing leading edge (Figure 1). The effects of both axial position (Figure 2) and vertical (Figure 3) position are considered. Furthermore, to enable the assessment of the effect of engine installation, a clean wing case for the aircraft and isolated engine cases are also evaluated. It is necessary to compare under-wing engines, clean-wing aircraft and isolated engine to fully appreciate the magnitude and nature of the installation effects.

Table 1 Matrix of vertical and horizontal positions of the fan cowl trailing edge

	dx/L_{nac}	dz/L_{nac}
A1	-0.453	-0.065
B1	-0.259	-0.065
C1	-0.065	-0.065
C2	-0.065	-0.129
C3	-0.065	-0.194

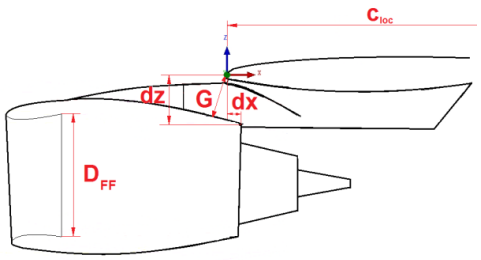

Figure 1 Sketch of key installation parameters

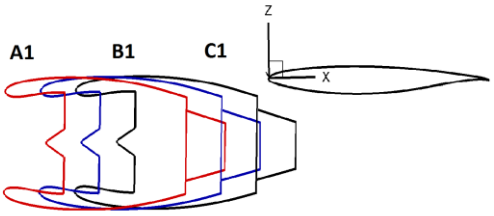

Figure 2 Sketch of horizontal positions of the engine in the presence of the wing of CRM

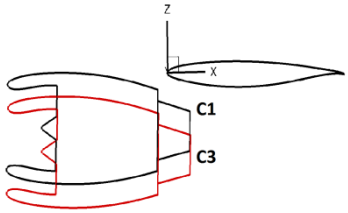

Figure 3 Sketch of vertical positions of the engine in the presence of the wing of CRM

B. Engine model

To provide a range of realistic boundary conditions for an engine, a thermodynamic engine performance model was required. The engine performance modelling was undertaken with use of the in-house code, Turbomatch[13]. Turbomatch is based on zero-dimensional aero-thermal analysis that uses discrete component maps. The employed method solves for the mass and energy balance between the various engine components. For the scope of the present work, the engine is assumed to be operating exclusively in steady-state conditions. Based on the CRM performance at M=0.82, a net thrust requirement at an altitude of 35000 ft. was estimated. Furthermore, an engine performance model for a typical modern turbofan-engine has been created to match the specification, and is referred to as the Baseline engine. Decisions on engine technology level were taken based on open source data for engines of comparable thrust class with an overall pressure ratio (OPR) of 50 and by-pass ratio (BPR) of 10. The engine performance model was used as a generator of engine boundary conditions to provide a realistic link between the engine intake and engine nozzles. The summary of investigated engine operating points is provided in Table 2, where the key engine operating conditions are intake massflow capture ratio (MFCR), fan pressure ratio (FPR), engine by-pass ratio (BPR), fan nozzle pressure ratio (FNPR), core nozzle pressure ratio (CNPR), turbine entry temperature (TET), and reference modified gross propulsive force (GPF^*_{ref}). A massflow capture ratio is the ratio of the flow area of pre-entry streamtube at upstream infinity (A_∞) divided by a geometrical intake area (A_{hi}). Moreover, the FNPR and CNPR are a ratio of nozzle total pressure to static ambient pressure.

Table 2 Key performance parameters for tested engine power settings

Power Setting	MFCR [-]	FPR [-]	FNPR [-]	CNPR [-]	GPF^*_{ref} [kN]
PS1	0.75	1.67	2.71	1.37	166.606
PS2	0.7	1.63	2.51	1.27	146.212
PS3	0.65	1.58	2.32	1.20	128.559
PS4	0.6	1.55	2.12	1.14	111.283

Based on the performance model of the Baseline engine, an axisymmetric geometry of an engine nacelle was created (Figure 4). Preliminary design guidelines were implemented to determine engine keypoints such as fan hub, fan tip, intake throat, intake highlight, nacelle maximum diameter, nacelle trailing edge, key dimensions of exhaust ducts. The keypoints were linked with use of class shape transformation (CST) curves[14, 15] to provide aerolines with smooth curvature distribution.

C. Computational method

The aerodynamic analyses were performed using a compressible RANS method. An implicit flow solver, Fluent, was used for the entire study with second order discretization for all terms. The Green-Gauss node based discretization was used and, based on the results from 4th Drag Prediction Workshop (DPW)[16, 17], the $k-\omega\ SST$ turbulence model was used[18]. The aircraft with an installed engine was located in the numerical domain with size of $100c_{ref}$ which was adopted based on the conclusions from the DPW (Figure 5)[16]. The domain was bounded by an x-z symmetry plane and pressure far-field condition with M=0.82 and flow conditions for ISA altitude of 35000ft. A complementary computation for an isolated engine was carried out with an exact numerical setup as used in the aircraft studies. The hemispherical domain with a size of 50 engine maximum diameters was adopted based on previous studies[19, 20, 21]. Half of the engine was computed with the domain bounded by a symmetry plane through the engine centre. The other bounds of the domain used the far-field boundary condition which allowed prescription of the freestream conditions and engine angle of attack. In both the engine isolated and aircraft studies, the engine model was represented by a pressure outlet with target massflow for the fan and by pressure inlets for the by-pass duct entry and low pressure turbine exit. All engine and aircraft walls were modelled as no-slip boundaries. Furthermore, a sensitivity to engine thrust setting was performed and the conditions were chosen based on the engine performance model. The engine boundary conditions were modified appropriately to represent the engine operating conditions in terms of the massflow capture ratio (MFCR), the fan nozzle pressure ratio (FNPR) and the core nozzle pressure ratio (CNPR) (Table 2).

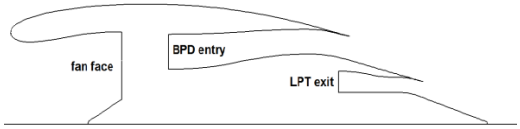

Figure 4 Sketch of the Baseline engine aerolines with key stations of the engine performance model marked such as fan face, by-pass duct entry, low-pressure turbine exit.

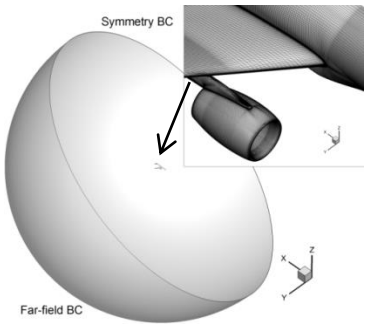

Figure 5 The hemispherical domain for aircraft studies and close-up on the surface mesh of the through-flow nacelle

D. Gridding methods

For the clean aircraft studies, the grid independence assessment followed the approach advocated by Roche[22]. Based on the gridding guidelines[16], a medium density structured mesh was created ("WBT0 medium" mesh) with an element count of around $10\text{x}10^6$ elements. Furthermore, four meshes were generated for the clean wing aircraft (WBT0) and the impact of spatial resolution on $C_{D\,A/C}$ was evaluated under a typical cruise conditions ($M_\infty = 0.85$ and $AoA = 2.5°$). The refinement ratio between the meshes was 1.15 in each direction. The boundary layer mesh was kept unmodified to have the same node distribution and the first cell height resulted in $y^+ = 1$ for all mesh densities. As a result, the meshes of $6.9\text{x}10^6$, $10.3\text{x}10^6$, $16.1\text{x}10^6$, and $24.1\text{x}10^6$ cells were created and referred to as "coarse", "medium", "fine" and "superfine" respectively. Richardson Extrapolation[23] was then conducted to estimate the grid independent solution. The aircraft drag coefficient $C_{D\,A/C}$ reduced monotonically with increasing mesh size. Using a factor of safety of 1.25, the second order grid convergence index (GCI) for a medium mesh solution was 2.05% and were within the asymptotic range with a GCI aspect ratio of 0.985. At the same time the second order grid convergence index (GCI) for fine mesh solution was 1.08% and were within the asymptotic range with a GCI aspect ratio of 0.992.

For the meshes with through flow nacelles (TFN), a structured mesh with a comparable blocking strategy to the clean wing case was created. Additional blocking was created to accommodate the presence of through flow nacelles. The blocking around the nacelle is arranged as an o-grid which is concentric with the engine axis. The meshing of the TFN geometry was based on the experience from the previous studies on isolated studies[19, 20, 21]. Thus, the following criteria have been added: 40 elements for the nacelle lip, maximum axial spacing on the nacelle $\Delta x = L_{nac}/110$. Those criteria have been merged with the DPW4 gridding guidelines[16] and the near wall treatment was facilitated with a $y^+ = 1$. In total, two mesh densities were used for the aircraft with a through flow nacelle and

the overall number of elements in the meshes are 22x10^6 and 30 x10^6. The meshes are called “medium”, “fine”, respectively. Also the meshes for the configurations with the TFN are derivations from the clean wing meshes where the applied modifications are localised around the TFN. On average the total drag value ($C_{D\,tot}$) increased by 0.2% for the fine mesh as compared with the medium mesh. Isolated nacelle configurations were modelled to enable a comparison between the nacelle with and without the presence of the wing. As a result a 7.2x10^6 element mesh for the through-flow nacelle in isolation was created by following the ‘fine mesh’ nacelle meshing rules as for the WBT0NP mesh. The size of the domain for the isolated TFN computation was adopted based on the experience from previous studies[20, 21] and it is the domain radius of 50 nacelle D_{max}.

Furthermore, the separate jet geometry is of key interest in the current research. The intake and nacelle meshing strategy was similar to that adopted for the TFN ‘fine mesh’. The nacelle meshing guidelines were established based on previous studies[24].However, the bypass duct, core duct, nozzles and core cowl required a modified blocking strategy for the computational mesh which also facilitated the boundary layer mesh. The CFD capabilities for the simulation of isolated engine configurations with separate exhaust systems were investigated by Vulgaris et al.[24], based on an open source test case[25, 26]. A set of 2D axisymmetric computation was carried for a range of power settings for the turbine power simulator (TPS). The mesh independence study for the TPS case was conducted with three grids and a constant refinement ratio of 1.5 was used. The medium for a 2D grid has around $1.6x10^3$ cells. The obtained GCI aspect ratio was 0.999 for all the surface integrals tested such as force on the core cowl, force on the fan cowl and force on the plug. As a result, it was considered that the asymptotic range was achieved. The separate-jet exhaust meshing criteria were developed based on the ‘fine’ mesh density and the 3D meshing guidelines were created by introduction of circumferential node distribution. For the domain study, further proprietary studies for the separate-jet configuration indicated an increase of the engine net propulsive force by +0.0032% between 40 and 50 nacelle D_{max} and +0.0008% between 40 and 60 nacelle D_{max}. Based on the previous experience, the meshing criteria for the separate-jet exhaust system were established and incorporated into the existing meshing criteria for nacelles. Moreover, the 3D engine blocking for an isolated engine with a separate jet exhaust was created that facilitated the boundary layer mesh blocks. The extent of the domain size was set to $50D_{max}$. As a result a mesh with 9.8 x10^6 elements was created for an isolated baseline engine with separate-jet exhaust and the meshing strategy is consistent with the ‘fine’ mesh resolution in the aircraft studies.

For the full engine geometry under the wing, the meshing strategy was similar to that adopted for the TFN under the wing. Similarly as for the isolated separate jet configuration, the mesh had to facilitate the boundary layer meshes for the bypass duct, core duct, nozzles and core cowl. The inclusion of the separate jet meshing rules resulted in the nominal mesh of 35 x10^6 elements that was derived from fine mesh for the clean wing configuration.

E. Drag accounting methods

For current work, an appropriate thrust and drag book-keeping system has to be followed[19, 20, 21, 27, 28]. As a result, a modified near-field method for separate jet engines is used (Figure 6). The forces that act in the thrust domain, i.e. on the inside of the streamtube, are denoted as θ and the forces in the drag domain are denoted as ϕ. Furthermore, gauge stream forces of the flow are denoted F_G

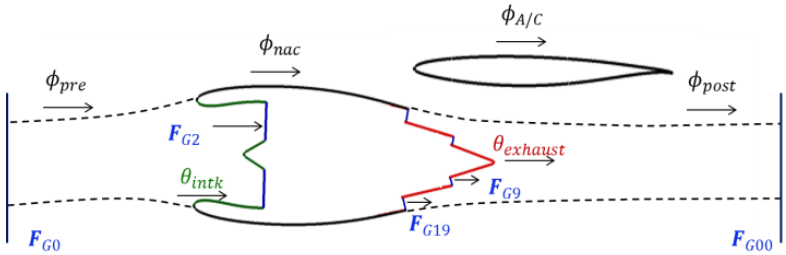

Figure 6 Decomposition of modified Near Field Method forces acting on the entry streamtube and nacelle.

The modified near-field method relies on the integration of the stream forces for the pre-entry stream tube and the summation of pressure and viscous forces that act on the cowl. Furthermore, the integration of stream forces for the post-exit stream tube and the summation of pressure and viscous forces that act on the core cowl and plug is considered. To account for all forces for an isolated or wing-installed engine, the Net Propulsive Force (NPF) is

considered as the difference of the overall engine thrust (F_{ov}) and nacelle drag (D_{nac}) along the drag aero-axis (Equation (1)). From the balance of forces for the post-exit domain, the unknown values of F_{G00} and ϕ_{post} from Equation (1) were substituted by known terms of stream forces (F_{G9} and F_{G19}) and fluid forces exerted on exhaust surfaces ($\theta_{exhaust}$). As a result, the NPF can be expressed in terms of standard net thrust (F_N) and fluid forces that act on the exhaust surfaces ($\theta_{exhaust}$), forces on the nacelle (ϕ_{nac}) and force on the pre-entry streamtube (ϕ_{pre}) (Equation (2)). By introduction of modified standard net thrust (F^*_N) and modified standard drag for the nacelle (D^*_{nac}) (Equations (3) (4)), the NPF can be expressed with (F^*_N) and (D^*_{nac}) terms alone (Equation (5)). For the analysis of the fan and core nozzles only, a gross propulsive force (GPF_ξ) in the engine axis is considered and defined (Equation (6)) as the summation of stream tube forces at nozzle exits (F_9 and F_{19}). Also a modified gross propulsive force is considered and defined (Equation (7)) in terms of the GPF_ξ which is modified by the pressure and viscous forces projected to the drag axis that act on the external surfaces of the exhaust. Furthermore, a modified drag coefficient can be defined (Equation (8)). Also the near-field method drag for the airframe ($D_{A/F}$) was evaluated by the integration of pressure and viscous forces on the surfaces of the wing, body, tail and an airframe drag coefficient (Equation (9)) was computed. Both $C_{D\,A/F}$ and $C_{D^*\,nac}$ are used for the computation of the aircraft total drag coefficient (Equation (10)). Similarly, a total lift coefficient for the aircraft is also obtained (Equation (11)). For the coefficients, the freestream reference condition is used, where ρ is the mass density of the fluid, υ is the velocity of the fluid and A_{ref} is the aircraft reference area. Overall the magnitude of the installation effect is considered as a difference of drag coefficients between the wing-installed nacelle or engine (installed) and the clean-wing (clean) configurations at constant lift (Equation (12)).

$$NPF = F_{ov} - D_{nac} = F_{G00} - F_{G0} - \phi_{pre} - \phi_{nac} - \phi_{post} \tag{1}$$

$$NPF = F_N - \theta_{exhaust} - \phi_{pre} - \phi_{nac} \tag{2}$$

$$D^*_{nac} = \phi_{pre} + \phi_{nac} \tag{3}$$

$$F^*_N = F_N - \theta_{exhaust} \tag{4}$$

$$NPF = F^*_N - D^*_{nac} \tag{5}$$

$$GPF_\xi = F_9 + F_{19} \tag{6}$$

$$GPF^*_\xi = F_9 + F_{19} + \theta_{exhaust} \tag{7}$$

$$C_{D^*\,nac} = \frac{D^*_{nac}}{\frac{1}{2}\rho v^2 A_{ref}} \tag{8}$$

$$C_{D\,A/F} = \frac{D_{A/F}}{\frac{1}{2}\rho v^2 A_{ref}} \tag{9}$$

$$C_{D\,tot} = C_{D\,A/F} + C_{D^*\,nac} \tag{10}$$

$$C_{L\,tot} = C_{L\,A/F} + C_{L^*\,nac} \tag{11}$$

$$\Delta C_{D\,inst|CL} = \left[C_{D\,(installed)} - C_{D\,(clean)}\right]_{C_L=const} \tag{12}$$

III. Results

A. Validation

Currently, there is no publicly available validation test-case that represents a separate-jet engine under the wing. However, a reasonable amount of work in the current research was dedicated to the development of the necessary building blocks that would increase credibility in the computational methods and allow for the investigation of the installation effects of the under-wing engines. The validation work was carried out to indicate the ability of CFD in determination of aircraft aerodynamic performance and it is discussed in the first validation subsection. Furthermore, the aerodynamics of through-flow nacelle installations were investigated to determine if CFD can

capture the changes to drag and lift of the aircraft, as well as the detailed effect in pressure distributions on the wing. The effects of TFN installation are summarised in the second validation subsection

1. Clean wing aircraft

To assess the ability of the CFD method in assessing the aircraft aerodynamics it was decided to base the work on the relatively modern airframe of the NASA CRM[10]. The aerodynamics for the CRM with and without Through Flow Nacelles (TFN) has been experimentally investigated[11, 12] using a 1/37th sub-scale model at a Reynolds number of 5x10^6. The clean aircraft (WBT0) lift-drag polar for the coarse, medium and fine meshes were compared with the experimental data as well as with the results from the 4th Drag Prediction Workshop[17] (Figure 7). At the cruise design point ($C_L = 0.5$), the calculations are within approximately 12dc from the measurements. Overall the computational results are similar to those reported in the DPW by Rivers et al. [11] and Tinoco et al [17].

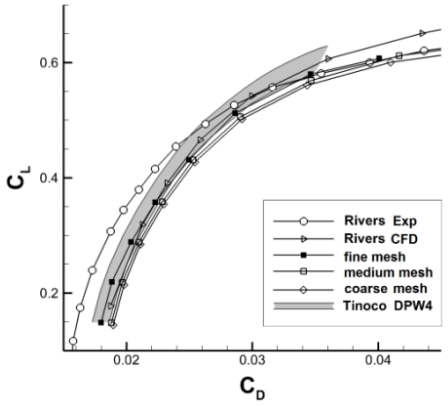

Figure 7 Computational drag polar for a rigid clean wing CRM (WBT0) for, 'coarse mesh', 'medium mesh' and 'fine mesh' compared with computational data for rigid geometry by Rivers et al. [11]; All data compared with measurements[11]. Band of structured-mesh solutions with use of $k-\omega$ SST and S-A models as from 4th Drag Prediction Workshop marked in grey[17]. All data at Re=$5x10^6$ and $M_\infty = 0.85$; all current CFD with $k-\omega$ SST

2. The effect of a through-flow nacelle

To evaluate the capability of CFD in the assessment of installation drag, the clean wing aircraft (WB) and the aircraft with through flow nacelle (WBNP) were computed. The installation of the TFN caused an increase of drag coefficient across a range of lift coefficients from approximately 0.15 to 0.5. The equal drag point between configurations with and without nacelle was at about $C_{L\,tot} = 0.6$. The computations broadly captured (Figure 8) the magnitude of +25 to +35 dc for installation drag $\Delta C_{D\,inst|CL}$ (Equation (12)) and the magnitude was roughly constant across the range of $C_{L\,tot}$ from 0.15 to 0.55. For higher $C_{L\,tot}$, a dramatic change of behaviour of $\Delta C_{D\,inst|CL}$ was observed with a reduction of up to -95dc for both computation and measurements.

Clearly the TFN can have a notable impact on the overall changes in C_D and C_L. It is also of interest to consider how the TFN affects the more local aerodynamics of the wing. The presence of the TFN changes the pressure coefficient distribution mostly at measurement stations closest to the installation such as spanwise position $\eta = 0.283$. As a datum, it was chosen to present the C_p distributions for the clean wing (WB) configuration for the computations and the measurements at M=0.83 and equal lift of $C_L = 0.5$ (Figure 9). Based on the limited available measurements, the effect of the TFN installation on the pressure distribution was considered for the configurations with (WBNP) and without the nacelle (WB) at a constant angle of attack of $AoA_{EXP} = 2.87°$ (Figure 9). The purpose of this comparison is to indicate the loss of lift and the change in the pressure distribution due to the installation. Furthermore, the C_p distributions for the computations of the WBNP configuration were considered (Figure 9). Ideally, the comparison between the computations and measurements for WBNP would be done at a constant lift coefficient, but the closest available data were for $(C_L)_{WBNP\,CFD} = 0.483$ and $(C_L)_{WBNP\,EXP} = 0.479$, respectively. Although there is a difference of $\Delta C_L = 0.004$, it is estimated that this equates to a difference in maximum ΔC_p of 0.0047. This is significantly smaller that the $\Delta C_p = 0.1$ due to the effect of the TFN installation.

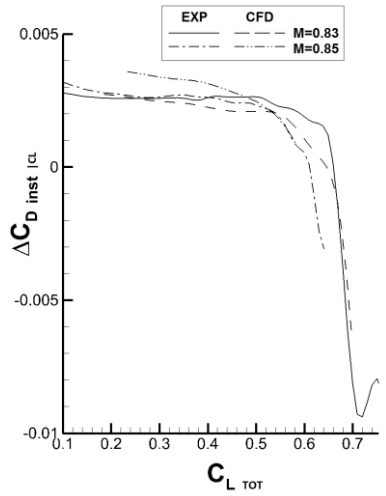

Figure 8 Installation drag coefficient (ΔC_{Dinst}) for CRM WB and WBNP as a function of lift coefficient; comparison between CFD medium mesh and experimental data by Rivers et al[11] for Mach number of 0.83 and 0.85; $Re = 5x10^6$

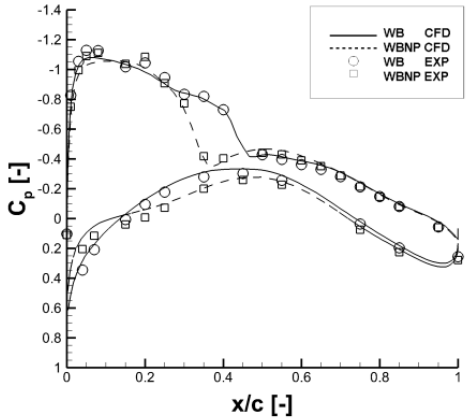

Figure 9. Comparison of pressure distribution C_p for CRM with (WBNP) and without the TFN (WB) at $Re = 5x10^6$; $M = 0.83$; $\eta = 0.283$; Computation with $k - \omega$ SST fully turbulent; Clean wing (WB) $C_L = 0.5$ for both experimental[11] and numerical; The experimental comparison between WB and WBNP at constant angle of attack $AoA_{EXP} = 2.87°$; The numerical comparison between WB and WBNP at constant angle of attack $AoA_{EXP} = 2.5°$.

Based on the experimental results for the wing cross-section closest to the engine installation ($\eta = y/(b/2) = 0.283$; Figure 9), there are clear effects of the TFN installation on the pressure distribution. The key difference is that the position of the shock moved forward from x/c=0.45 for the clean wing to x/c=0.35 when with TFN. There is evidence of the impact of the TFN on the pressure side (Figure 9), where there is a reduction of the pressure coefficient inboard from the pylon, followed by an increase of pressure coefficient after the nacelle trailing edge at x/c=0.15. The change of pressure coefficient is approximately $\Delta C_p = \pm 0.1$. Further aft on the pressure side at x/c=0.7 the pressure distribution for both configurations (WBT0 and WBT0NP) are broadly unaffected. Although the computations tended to under-predict the suction peak value of pressure coefficient by $\Delta C_p = -0.1$ (Figure 9), the under-prediction was consistent between the clean wing configuration and configuration with the TFN. Moreover, the location of the shock was shifted by $\Delta x/c = -0.1$ due to installation and the exact shock location was captured correctly for both geometrical configurations. As well as for the suction side, the computation for the pressure side of the wing is in a good agreement with measurements. The CFD captured correctly the magnitude of flow acceleration in the gulley between the wing and the nacelle with maximum $\Delta C_p = +0.15$ at x/c=0.05 (Figure 9). Overall, the CFD results indicate similar characteristics to the experimental data.

B. Effect of engine installation on aircraft aerodynamics for the datum engine position

To study the effect of incidence on the engine installation effects, the CRM with under-wing engine in baseline position C3 (Table 1) is considered. The engine installation under the wing notably affects the performance of an aircraft in both the drag and thrust domain. In addition, the installation effects are a function of aircraft angle of attack. As for the drag domain, the presence of the engine caused an increase of aircraft total drag (Figure 10) across almost the entire range of angles of attack from 0° to 5°. The drag penalty increased from 25dc at $C_L = 0.2$ to 34dc at C_L=0.5. Moreover, at a given angle of attack, the configuration with an engine had a reduced lift coefficient in comparison with the clean wing configuration (Figure 10). Both the increase in drag and reduction in lift are a result of a notable interaction between the wing and the engine as observed in the flow-field (Figure 11).

The loss of lift by roughly $\Delta C_{L\,inst} = -0.02$ (Figure 10) is caused by the reduction of local angle of attack and mainly by a reduction in suction on the wing upper surface (Figure 12). In addition, an observable flow acceleration

in the range of $\Delta C_p = -0.25$ is present close to the wing leading edge on the lower side of the wing, whereas the suction at the maximum profile thickness reduces by $\Delta C_p = +0.2$. By integration of pressure and viscous forces in individual cross-sections of the wing it is possible to obtain the span-wise lift distribution (Figure 13). The installation of the nacelle predominantly affects the inboard side of the nacelle ($y/(b/2) < 0.3$), where the local loss of lift coefficient was roughly 0.05 for a typical aircraft cruise incidence $AoA_{A/C} = 2.5°$. Moreover, outboard of the nacelle the effect of installation on the local lift coefficient diminishes and beyond $y/(b/2) > 0.6$ it drops below 0.01.

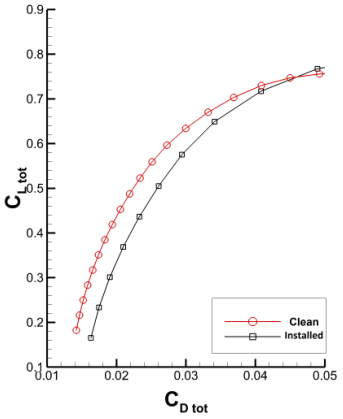

Figure 10 The lift and drag polar for the CRM without (Clean) and with (Installed) the engine in position C3 in power setting "PS1"; $Re = 45x10^6$; $M_\infty = 0.82$;

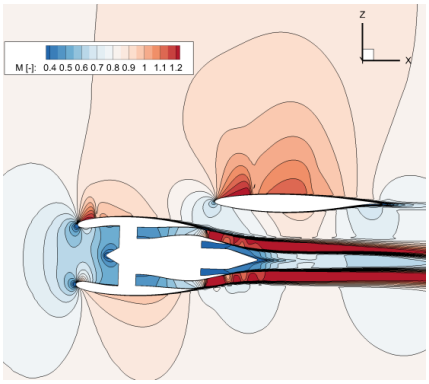

Figure 11 Contours of Mach Number at the spanwise cross-section through the engine axis in position C3 in power setting "PS1"; $AoA_{A/C} = 2.5°$; $Re = 45x10^6$; $M_\infty = 0.82$

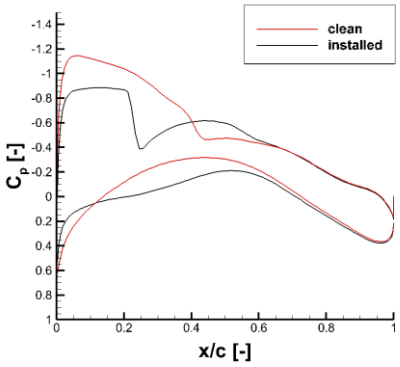

Figure 12 The pressure coefficient distribution at span-wise cross-section at $y/(b/2)$=0.3 for CRM with (installed) and without (clean) engine at $AoA = 2.5°$; $Re = 45x10^6$; $M_\infty = 0.82$

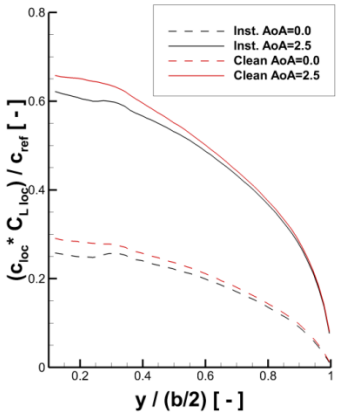

Figure 13 The spanwise distribution of non-dimensional lift coefficient ($C_{L\,loc}c_{loc}/c_{ref}$) for CRM with (installed) and without (clean) engine at $AoA_{A/C} = 0.0°$ and $AoA_{A/C} = 2.5°$; $Re = 45x10^6$; $M_\infty = 0.82$

The pressure distributions at the top-line of the fan cowl are compared between the wing-installed and an isolated engine (Figure 14). To provide a fair comparison between these configurations, it is necessary to make the evaluations at similar incidences. For the installed configuration the local engine incidence is taken as the sum of the aircraft angle of attack and the engine installation angle (AoA_{inst}). For the CRM configurations $AoA_{inst} = +1.75°$. Therefore at each aircraft angle of attack ($AoA_{A/C}$) the comparisons were made with the equivalent isolated engine configuration taking the additional AoA_{inst} into account.

Moreover, in reality the engine is present in the flow-field distorted by the presence of the wing and as a result the local angle of attack deviates from the nacelle incidence (AoA_{eng}). The deviation between local angle of attack and the aircraft global angle of attack due to the wing pressure field is the up-wash angle (AoA_{upwash}). For the current

comparison, the up-wash angle was determined based on the clean wing configuration at the point where the centre of the engine highlight would be in the engine-aircraft configuration. Based on the datum case the up-wash angle increases relatively linearly from $-0.1°$ at $AoA_{A/C} = 0°$ to roughly $= 0.6°$ at $AoA_{A/C} = 2.5°$. It is determined that the effect of the up-wash is localised mostly at the forebody of the fan cowl (Figure 14). At a local engine incidence of approximately $AoA_{eng,ideal} = 1.75°$ the installed engine presents a reduction in the peak suction at the forebody by $\Delta C_p = -0.05$ as compared with the isolated engine, where the up-wash was evaluated to be $AoA_{upwash} = -0.1°$. An increase in engine local incidence ($AoA_{eng,ideal}$) results in a neutral up-wash effect and as a result the peak suction at the fancowl forebody between the isolated and wing-installed engine is equal in magnitude $C_p = 0.7$ at $\xi/L_{nac} = 0.1$ at $AoA_{eng} = 2.75°$ (Figure 14). A further increase in local engine incidence results in the increasing effect of the up-wash and as a result a $\Delta C_p = +0.05$ is noted for the wing-installed engine as compared with the isolated engine. It has to be noted that the effect of the up-wash is localized in the forebody and the pressure distributions exhibit no difference at $\xi/L_{nac} = 0.3$ (Figure 14) for both isolated engine with $C_p = -0.4$ and for the wing-installed with $C_p = -0.35$. Beyond the point of $\xi/L_{nac} > 0.3$ (Figure 14) the isolated engine is exposed to an additional pressure force generated as a result of the change of the jet direction to align with the ambient flow. The magnitude of this increase is $\Delta C_P = +0.047$ at $\xi/L_{nac} = 0.7$ (Figure 14) across the entire investigated range of incidence from $AoA_{eng,ideal}1.75°$ to $AoA_{eng,ideal} = 4.75°$.

Furthermore, the increase of positive pressure at the aft of the fan cowl is also observed for the wing-installed engine (Figure 14). However, the magnitude of the increase of this beneficial pressure force is greater and equals $\Delta C_P = +0.03$ for every degree of increased incidence ($AoA_{eng,ideal}$). The significant increase of the forward oriented force is explained by the the pressure field perturbation and the force provides a beneficial reduction of the nacelle drag (D^*_{nac}). The effect of the buoyancy force on the aft of the fan cowl, and the contribution of the suction on the nacelle leading edge sum up to a single forward oriented force (Fig. 14). As a result, as the aircraft angle of attack increased the modified drag of the installed engine (D^*_{nac}) reduced from 45dc at $AoA_{A/C} = 0°$ to 20dc at $AoA_{A/C} = 4.5°$. Moreover, it was assessed that the changes to the nacelle viscous forces due to incidence are broadly negligible and that the pressure field effects were the dominant terms. Relative to the isolated engine, the changes in pressure distribution over the nacelle lead to an overall nacelle drag reduction for wing-installed nacelle of approximately 10dc at a typical cruise incidence $AoA_{eng,ideal} = 4.25°$. Furthermore, as expected, the tail and fuselage component were not affected by the installation of the engine.

$$AoA_{eng,ideal} = AoA_{A/C} + AoA_{inst} \tag{13}$$

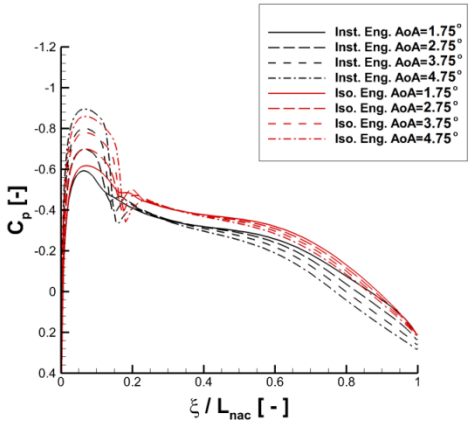

Figure 14 Pressure coefficient distribution at topline of the fan cowl for installed engine at given aircraft angles of attack ($AoA_{A/C}$), compared with isolated engines at its angle of attack (AoA_{eng}); $Re = 45x10^6; M = 0.82$;

The installation of the engine under the wing also affects the engine performance in the thrust domain as considered within the efflux streamtube. To quantify the effect, a gross propulsive force in the direction of the engine axis (GPF_{ξ}) (Equation (6)) was considered for both the isolated and wing-installed engine (Figure 15) and referenced to

$GPF_{ref} = 160462\ N$ of an isolated engine at power setting PS1 at $AoA_{eng} = 0°$. The gross propulsive force of an isolated engine was relatively insensitive to incidence. The installation of the engine under the wing results in a modest reduction of the gross propulsive force by approximately 0.1% at a typical cruise condition of $AoA_{A/C} = 2.5°$. Moreover, the installation effect on GPF_ξ was a function of aircraft angle of attack and GPF_ξ reduced by approximately 0.25% at $AoA_{A/C} = 4°$ as compared with the isolated engine. This was explained by a reduction of mass flow in the core nozzle and it was manifested in the similar trend of discharge coefficient (C_d^{core}) with incidence (Figure 16). The reduction in discharge coefficient was a result of the higher base pressure at the core nozzle and it was the consequence of the wing pressure-field. Meanwhile, the by-pass nozzle operated choked and there was little sensitivity of discharge coefficient to incidence and little effect to the installation (Figure 16). Furthermore, the modified gross propulsive force (GPF_ξ^*) was considered to take into account the forces which act on the external parts of the exhaust such as the core cowl and the plug. Even though, the external surfaces produce friction drag, the effect of the pressure forces dominates the balance and a beneficial forward oriented force was generated that contributed to an increase in GPF_ξ^* (Figure 15). For the isolated engine, the GPF_ξ^* is greater than GPF_ξ by 3.8% at $AoA_{A/C} = 0°$ and by 3.6% at $AoA_{A/C} = 4°$. The beneficial pressure force exerted on the external surfaces of the exhaust was the result of a higher than ambient local base pressure in the jet. Furthermore, due to the installation, the local base pressure of the engine interacted with the wing pressure field. At low aircraft incidence ($AoA_{A/C} = 0°$) the engine exhaust was exposed to the local flow acceleration that occurred below the lower side of the wing. As a result, at zero incidence, relative to the isolated engine there is a reduction of GPF_ξ^*/GPF_{ref} from 1.038 to 1.021. For the wing-installed engine, the GPF_ξ^* is sensitive to $AoA_{A/C}$ and rises monotonically as a result of the increase in wing loading. The positive pressure-field is generated on the lower side of the wing and is acts on the engine and effects GPF_ξ^* (Figure 15). At the cruise point of $AoA_{A/C} = 2.5°$, the installed and isolated GPF_ξ^* are almost the same while at $AoA_{A/C} = 4°$ the GPF_ξ^* for the wing-installed engine has increased by 0.3% as compared with the isolated engine.

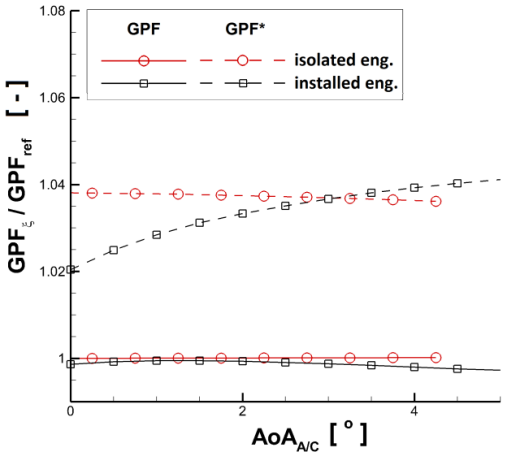

Figure 15 The overall gross propulsive force (GPF_ξ) for the Baseline engine in isolation and under the wing (installed) compared with the modified gross propulsive force (GPF_ξ^*); non-dimensionalised by GPF_ξ of an isolated engine at $AoA_{A/C} = 0°$ ($GPF_{ref} = 160462\ N$) $Re = 45x10^6; M = 0.82$;

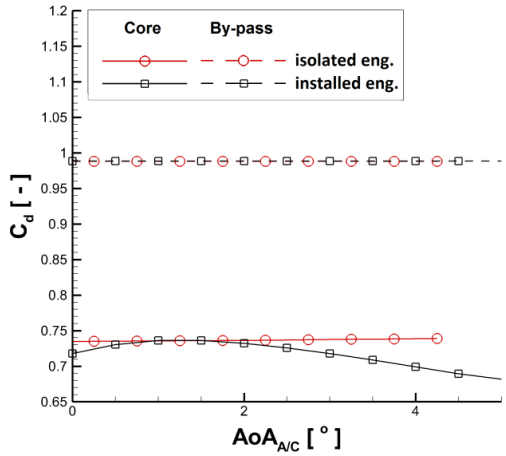

Figure 16 The discharge coefficient (C_d) for core nozzle and by-pass nozzle of the Baseline engine in isolation compared with the Baseline engine under the wing (installed); $Re = 45x10^6; M = 0.82$;

C. Effect of engine horizontal position on installation aerodynamics

The sensitivity of aircraft total drag to the engine relative position was investigated for a range of axial positions (Figure 2). The chosen positions are A1 (dx/L_{nac}=-0.453), B1 (dx/L_{nac}=-0.259) and C1 (dx/L_{nac} =-0.065) (Table 1). The change of the axial position had a significant effect on the aircraft total modified drag ($C_{D\,tot}$) (Figure 17). At typical cruise condition of $C_{L\,tot} = 0.5$, the installation drag ($C_{D\,inst|CL}$) is 43dc, 43dc and 38dc for A1, B1 and C1 respectively as compared with the clean wing aircraft. The difference in $C_{D\,inst|CL}$ between the configuration with different engine axial position is approximately 5dc at cruise lift coefficient of $C_L = 0.5$ and it corresponds to 2% of

total aircraft drag. Moreover, the difference in $C_{D\ inst|CL}$ across the range of axial positions at a lift coefficient of $C_L = 0.2$ is 15 dc.

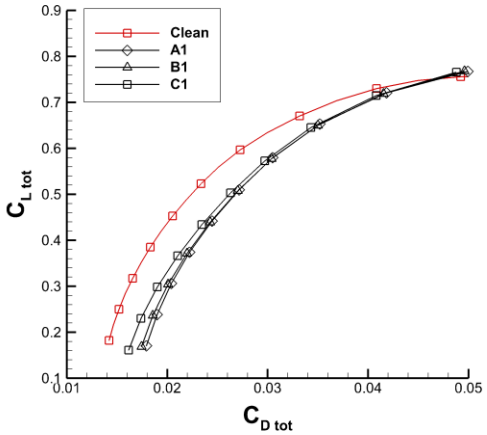

Figure 17 Lift-drag polar for CRM without (Clean) and with engine in three horizontal positions A1, B1 and C1; $Re = 45x10^6; M = 0.82$;

Furthermore, the engine in the close-coupled C1 position was clearly located in the positive pressure field from the wing (Figure 18 b). The effect on the nacelle was the buoyancy force that acted on the afterbody, whereas the wing experienced an acceleration in the gulley on the lower side of the wing from x/c=0.05 to x/c=0.2 (Figure 18b) as compared with clean wing (Figure 18 a). Even though the two other horizontal positions (B1 - Figure 18c) and (A1 - Figure 18d) exhibited less interaction between the nacelle and the wing compared with the C1 positon (Figure 18 b), there is an observable change in the flow field in relation to isolated engine (Figure 18e).

To compare the isolated engine with the wing-installed engines, there is a need to define the nacelle local incidence, at which the comparison can be performed. Therefore an idealised effective engine incidence ($AoA_{eng,\ ideal}$) is considered (Equation (13)) and equals $AoA_{eng,\ ideal} = 1.75°$ for the case at $AoA_{A/C} = 0°$ and $AoA_{eng,\ ideal} = 4.25°$ at typical cruise aircraft incidence of $AoA_{A/C} = 2.5°$. For the investigated horizontal engine positions the up-wash angle changed linearly from approximately $\alpha_{upwash} \approx 0.0°$ at zero aircraft incidence to $\alpha_{upwash} = +0.5°$ at the typical cruise condition $AoA_{A/C} = 2.5°$. An up-wash angle of 0.5° corresponds to approximately $\Delta C_p = +0.04$ and an increase in ΔC_{D^*nac} =0.2 dc. For the current comparison, the idealised engine incidence ($AoA_{eng,\ ideal}$) is used for simplicity.

Based on pressure distributions (Figure 19), the suction peaks at the nacelle top-line for the wing-installed engines at $AoA_{eng,\ ideal} = 1.75°$ ($AoA_{A/C} = 0.0°$) presented the same peak suction $C_p = -0.6$ at forebody as the isolated engine. As for the afterbody of the fan cowl, the B1 and A1 position were affected by an increase of pressure coefficient $\Delta C_p = +0.05$ in relation to isolated engine and the engine in the close-coupled position C1 was affected by $\Delta C_p = +0.1$. As the incidence increases to $AoA_{eng} = 4.25°$ ($AoA_{A/C} = 2.5°$) there is an increase of peak suction of $\Delta C_p = -0.07$, which is the result an up-wash of $AoA_{upwash} = +0.5°$ for all three engine positions (Figure 20). Moreover, the effect of the wing on all three positions on the central section ($\Delta\xi/L_{nac} = 0.5$) of the fan cowl is roughly $\Delta C_p = +0.05$ and there are only minor differences between the positions up to $\Delta\xi/L_{nac} = 0.7$. Only a slight movement of the shock downstream occurred as the engine was repositioned forward from the wing. In the afterbody section, the close-coupled position C1 observed an additional effect of $\Delta C_p = +0.05$ as compared with other positions A1 and B1 at $\Delta\xi/L_{nac} = 0.9$.

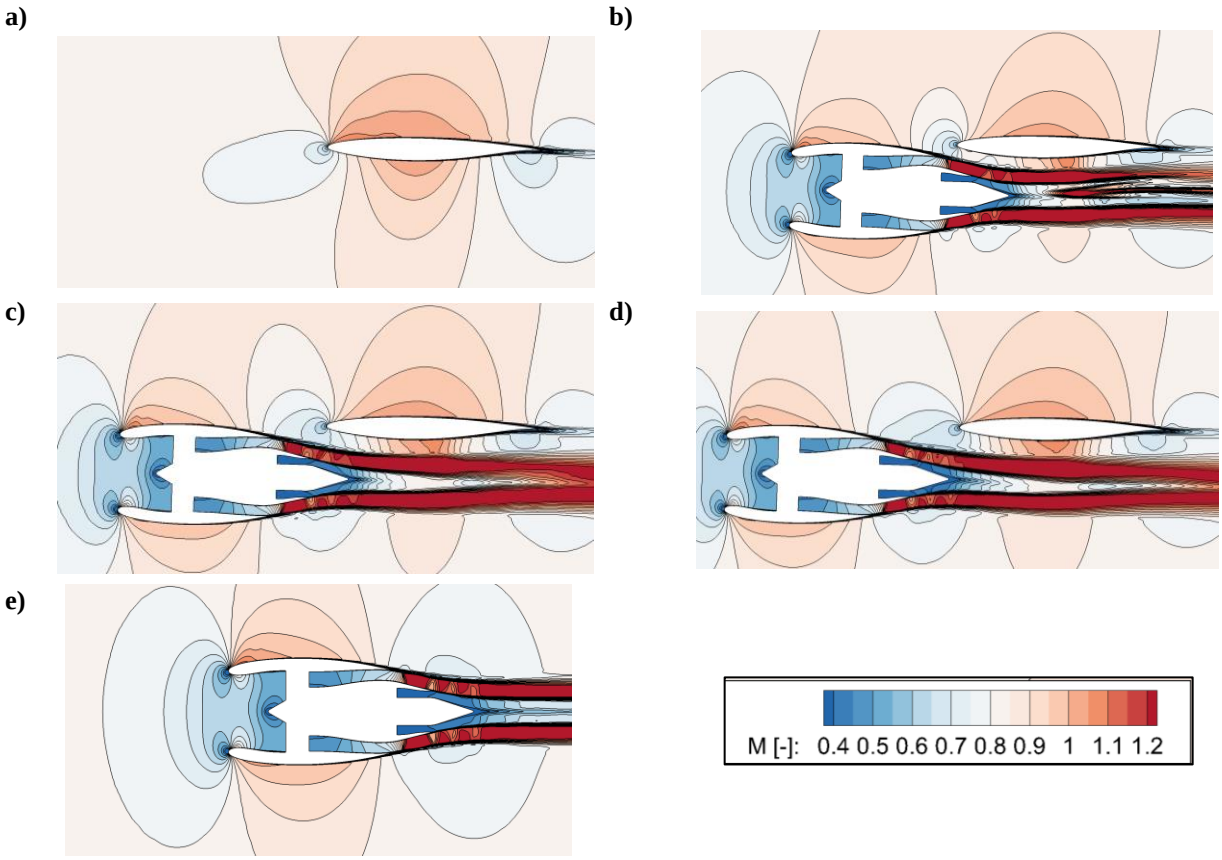

Figure 18 Contours of Mach Number at span-wise cross-section through the engine axis for a) Clean wing and three engine axial positions b) C1, c) B1, d) A1; $Re = 45x10^6$; $M = 0.82$; $AoA_{A/C} = 0°$, Compared with e) isolated engine at $AoA_{eng} = 1.75°$

Furthermore, due to the engine installation at $AoA_{A/C} = 0°$ (Figure 21), the suction on the upper side of the wing reduced by $\Delta C_p = +0.35$ for all three engine positions at $y/(b/2) = 0.283$. The major difference between the three horizontal engine positions was observed on the wing pressure side. The positions A1 and B1 positions shifted downstream the point of maximum suction as compared with the clean wing by $\Delta x/c = +0.1$ $\Delta x/c = +0.15$, respectively. Meanwhile, the C1 position experienced a completely different behaviour. The suction region for the C1 position had three local maxima of suction (Figure 21). The first peak was triggered by the partial overlap of the wing with an engine, the second peak was the result of local acceleration caused the flow from the by-pass and the third peak appeared at maximum thickness of wing profile. The change of the flow mechanism is caused by a partial overlap of the close-coupled configuration and it explained the significant differences between the close-coupled and other engine positions. As the aircraft incidence increased, the same mechanism for the closed-coupled position C1 is still observed, but the magnitude of the three local maxima reduced (Figure 22). As for the suction side, all three positions present broadly similar pressure distributions with a reduction in peak suction by $\Delta C_p = +0.3$.

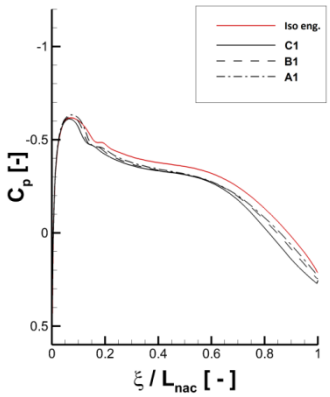

Figure 19 Pressure distribution at nacelle top-line ($\Theta = 0°$) for three engine positions (A1, B1 and C1) compared with an isolated engine for idealised engine incidence $AoA_{eng,ideal} = 1.75°$ ($AoA_{A/C} = 0°$); $Re = 45x10^6$; $M = 0.82$;

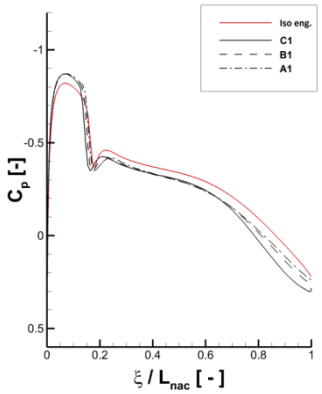

Figure 20 Pressure distribution at nacelle top-line ($\Theta = 0°$) for three engine positions (A1, B1 and C1) at $AoA_{A/C} = 2.5°$ compared with an isolated engine for idealised engine incidence $AoA_{eng,ideal} = 4.25°$ ($AoA_{A/C} = 2.5°$); $Re = 45x10^6$; $M = 0.82$;

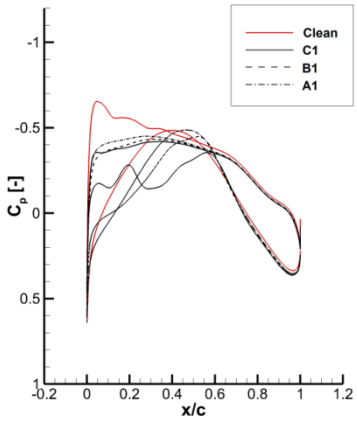

Figure 21 Pressure distribution at wing cross-section at engine installation plane ($y/(b/2) = 0.283$) at $AoA_{A/C} = 0°$ for three engine positions (A1, B1 and C1) compared with clean wing configuration; $Re = 45x10^6$; $M = 0.82$;

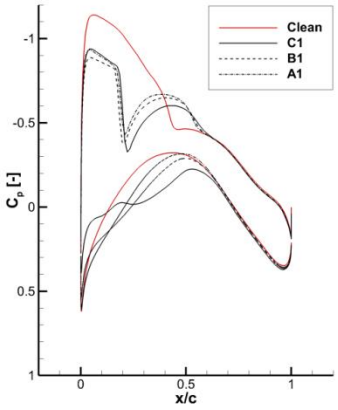

Figure 22 Pressure distribution at wing cross-section at engine installation plane ($y/(b/2) = 0.283$) at $AoA_{A/C} = 2.5°$ for three engine positions (A1, B1 and C1) compared with clean wing configuration; $Re = 45x10^6$; $M = 0.82$;

Furthermore, the pressure (Figure 23) and viscous drag coefficients for the wing and the nacelle surfaces were computed. The interaction between the wing and the nacelle resulted in the reduction of pressure drag computed at the wing for the C1 position (Figure 23) and an increase of pressure drag computed at the wing for the B1 and A1 positions in relation to the clean wing configuration. The increase in wing pressure drag was 35dc for a movement of the engine from C1 to A1 at low incidence $AoA_{A/C} = 0°$ and roughly 20 dc at a typical cruise incidence of $AoA_{A/C} = 2.5°$. The reduction of wing drag for close-coupled positon C1 is explained as an increased suction on the pressure side of the wing near the wing leading edge. Meanwhile, the viscous forces remained insensitive to axial changes of the engine position. Furthermore, to appreciate the 3D nature of the mechanism, the lower surface of the wing (Figure 24a) and the surfaces of the fan cowl, core cowl and plug were unwrapped to be presented in 2D form (Figure 24b), Figure 24c), Figure 24d). Even though the close-coupled configuration (C1) (Figure 24b) had an increased pressure at the top of the nacelle afterbody ($\Theta = 0°$) in relation to two other configurations (A1, B1) (Figure 24c), Figure 24d), the inboard (Θ from 0° to -180°) of the nacelle afterbody was subject to increased acceleration that resulted in a detrimental increase of pressure drag at zero aircraft incidence ($AoA_{A/C} = 0°$).

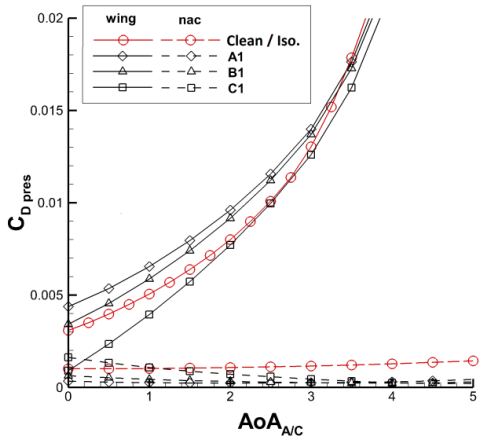

Figure 23 Pressure drag coefficient as a function of aircraft angle of attack for Clean wing aircraft, isolated nacelle and three engine positions (A1/B1/C1); $Re = 45x10^6$; $M = 0.82$;

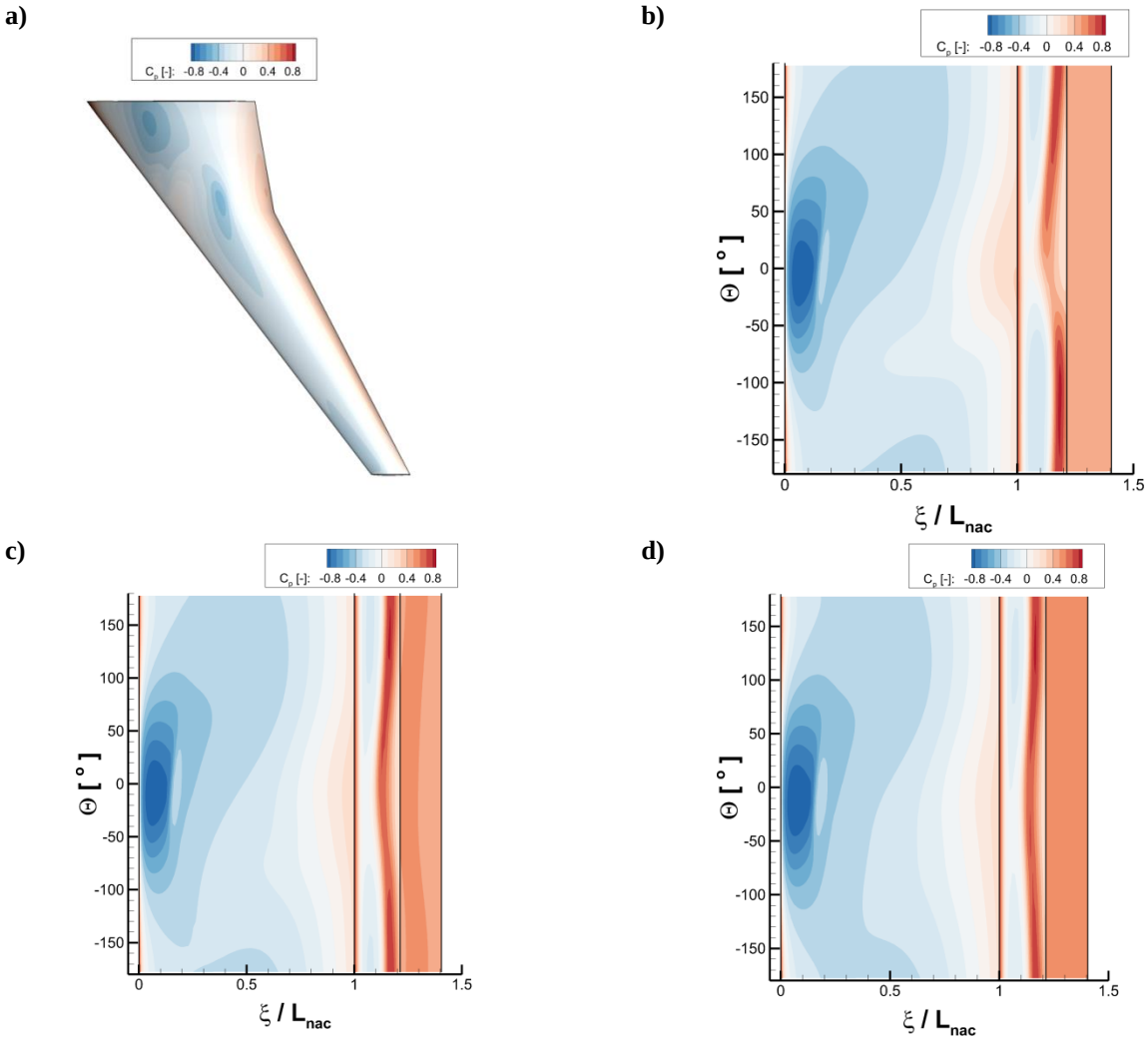

Figure 24 Contours of pressure distribution C_p on a) the wing in presence of the engine in position C1 viewed from the underside. Contours of pressure distribution on unwrapped surfaces of fan cowl, core cowl and plug for engines in position: b) C1, c) B1 and d) A1; $AoA_{A/C} = 0°$; $Re = 45x10^6$; $M = 0.82$; nacelle inboard for $\Theta < 0°$

The presence of the wing has an impact on the engine efflux. At $AoA_{A/C} = 0°$, the suction on the lower side of the wing draws the engine jet upward and changes the jet structure for the close-coupled configuration C1 (Figure 18b) in comparison with the isolated engine (Figure 18e). Moreover, the effect was sensitive to engine axial position, as for B1 and A1 positions (Figure 18c and d) the jet structure remained intact and resembled more the jet structure of an isolated engine (Figure 18 e). The efflux of an uninstalled engines typically exhibits expansion and compression waves in the bypass jet (Figure 18 e), which affects the pressure distribution at the core cowl of the engine (Figure 25). The increase of base pressure at the nozzle exit due to the wing pressure-field resulted in the reduction of the expansion at $\xi/L_{core} = 0.2$ by $\Delta C_p = +0.075$ and $\Delta C_p = +0.125$ for A1 and B1 respectively. Similarly the strength of the compression at $\xi/L_{core} = 0.7$ was reduced by $\Delta C_p = -0.1$ and $\Delta C_p = -0.15$ for A1 and B1 respectively. The C1 position of the engine exhibited a different characteristic, where the typical jet pattern was dominated by the pressure interaction from the wing (Figure 24b). The inboard section of the core cowl between $\Theta = 0°$ and $\Theta = -60°$ was dominated by a negative pressure distribution as a result of exposure of the inboard core cowl to a local acceleration (Figure 24b) on the wing. The B1 and A1 position were located further upstream and were less sensitive to the effect of partial overlap (Figure 24c) and Figure 24d). Overall, the change in the base pressure at the nozzle exit reduces the gross propulsive force (GPF_ξ) of the engine (Figure 26) by roughly 0.5% at typical cruise condition $AoA_{A/C} = 2.5°$ in relation to the GPF of the isolated engine at $AoA_{A/C} = 0°$. The effect depended on the engine position and wing loading. Moreover, the positive pressure field of the wing acted on the surfaces of the engine core cowl and engine plug and increased the modified gross propulsive force (GPF^*_ξ) for the position A1 by 0.6% at $AoA_{A/C} = 2.5°$ in relation to the isolated engine. The close-coupled position C1 exhibits the loss of GPF^*_ξ by 0.1% at $AoA_{A/C} = 2.5°$ in relation to the isolated engine as a result of close coupling and flow accelerations between the engine and the wing. The greatest impact on the GPF^*_ξ of the engine in the position C1 reaches -2% and is at aircraft incidence of $AoA_{A/C} = 0°$.

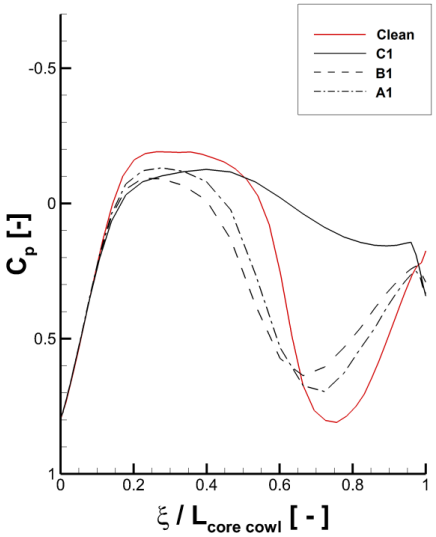

Figure 25 Pressure distribution at top-line ($\Theta = 0°$) of engine core cowl for three engines (C1, B1 and A1) compared with an isolated engine at comparable incidence. Engine installation angle $AoA_{inst} = 1.75°$.

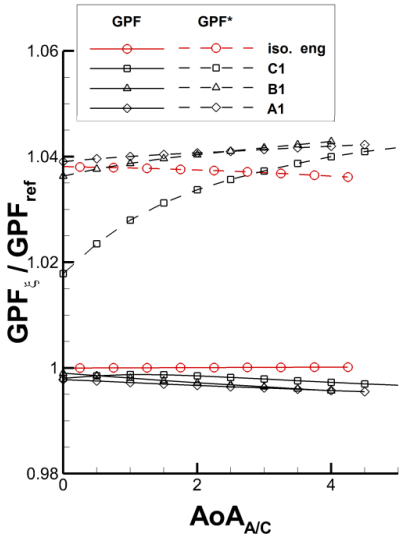

Figure 26 Specific gross propulsive force (GPF_ξ) and modified gross propulsive force (GPF^*_ξ) for isolated nacelle compared with three engine positions (C1, B1 and A1) along engine axis ξ; $Re = 45x10^6$; $M = 0.82$;

D. Effect of engine vertical position on installation aerodynamics

To investigate the effect of engine vertical position, the installed baseline engine at power setting PS1 (Table 2) was simulated at M=0.82 and $Re = 45x10^6$ for a range of $AoA_{A/C}$ from 0° to 5°. The installation of the engine in positions from C1 to C3 (Table 1) resulted in an increase of installation drag ($C_{D\,inst|CL}$) by approximately 20dc (Figure 27) as compared with the clean-wing aircraft at $C_{L\,tot} = 0.2$. Moreover, the differences between the configurations are modest in terms of $C_{D\,tot}$ at low values of $C_{L\,tot} < 0.4$. However, at typical cruise condition of $C_{L\,tot} = 0.5$, the installation drag is 38dc, 39dc and 34dc for C1, C2 and C3 respectively. In context of 1dc precision

for drag assessments, the positions C1 and C2 performed comparably, while the position C3 is significantly better than the others. To complement the analysis, the GPF_{ξ} and GPF_{ξ}^{*} were calculated over the range of aircraft incidence (Figure 28). As for the GPF_{ξ}, at a typical cruise incidence $AoA_{A/C} = 2.5°$ a reduction of 0.2% is observed for all three positions in comparison with the isolated engine and it is explained by the effect of the pressure-field on the core nozzle. At the same $AoA_{A/C} = 2.5°$, the GPF_{ξ}^{*} increased as compared with isolated engine by 3.56%, 3.55% and 3.51% for positions C1, C2 and C3 respectively.

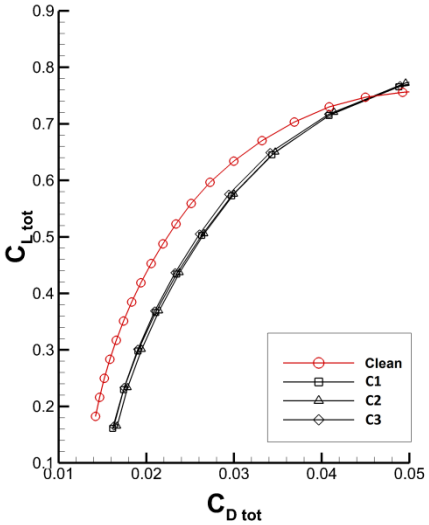

Figure 27 A lift-drag polars for baseline engine (PS1) in three vertical positions (C1, 'C2' and C3) compared with a clean-wing configuration; $Re = 45x10^{6}; M = 0.82$;

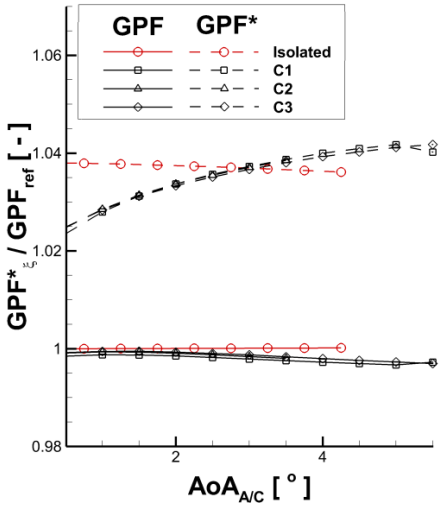

Figure 28 Specific gross propulsive force (GPF_{ξ}) and modified gross propulsive force (GPF_{ξ}^{*}) for isolated nacelle compared with baseline engine (PS1) in three vertical positions (C1, 'C2' and C3); $Re = 45x10^{6}; M = 0.82$;

E. Effect of engine power setting on the installation aerodynamics

The impact of the engine power setting on the engine installation effects was analysed in the baseline position (C3) (Figure 29). The engine power setting was modified in the performance model by the prescription of a range of turbine entry temperatures (TET). As a result engine operating points were obtained as listed in Table 2. Furthermore, the aerodynamic analysis was performed and it was recognised that there were 3 key parameters (Table 2) that dominated the aerodynamics, mass flow capture ratio (MFCR), fan nozzle pressure ratio (FNPR) and core nozzle pressure ratio (CNPR). The reduction of engine power setting reduced the massflow that comes into the engine and as a result the intake massflow capture ratio (MFCR) of the engine changed. The MFCR gives an indication of intake spillage characteristic. For the isolated engine, the effect of spillage is modestly sensitive to the engine incidence ($AoA_{eng,ideal}$) (Figure 30). The trend of the $C_{D^{*}nac}$ for an isolated engine is not affected by the reduction in power setting and the $C_{D^{*}nac}$ increases by 6dc at $AoA_{eng,ideal} = 1.75°$ and 11dc at $AoA_{eng,ideal} = 7°$ over the range of power settings. Clearly the under-wing installation of the engine has a significant effect on the drag ($C_{D^{*}nac}$) characteristics of the engine. The $C_{D^{*}nac}$ increased from 36dc for an isolated engine in PS1 at $AoA_{eng,ideal} = 1.75°$ to 45dc when installed. However, as the aircraft incidence increases and the wing loading is greater, there is a pressure force that acts on the afterbody of the fan cowl and reduces the $C_{D^{*}nac}$ of an wing-installed engine. For example, at $AoA_{eng,ideal} = 7°$ the $C_{D^{*}nac}$ reduces from 40 dc for an isolated engine in PS1 to only 19 dc when installed. Furthermore, the power setting of the engine was reduced for the engine under the wing. The reduction of the massflow capture ratio from 0.75 to 0.6 for the engine power settings from PS1 to PS4 in the baseline position (C3) resulted in an increase of the total aircraft drag ($C_{D^{*}nac}$) by roughly 7 dc at $AoA_{eng,ideal} = 1.75°$ (Figure 29). The increase of $C_{D^{*}nac}$ across the range of PS1 to PS4 is monotonic. The increase of drag $\Delta C_{D^{*}nac}$ due to a reduction in power setting for the wing-installed engine is moderately dependent on the aircraft incidence (Figure 30). For an increase of incidence from $AoA_{eng,ideal} = 1.75°$ to $AoA_{eng,ideal} = 6.75°$ the $\Delta C_{D^{*}nac}$ increased slightly from 7 to 12dc over the entire range of power settings. It is suggested that the spillage characteristic is broadly unaffected by the installation due to the position of the intake outside of the wing pressure-field. However, the overall trend of the $C_{D^{*}nac}$ is a combination of the effect of the wing pressure field and the

spillage characteristics of an intake. Overall, the sensitivity of drag penalty due to the installation is 3 dc across the range of power settings, as a result of favourable aerodynamic effects on the airframe.

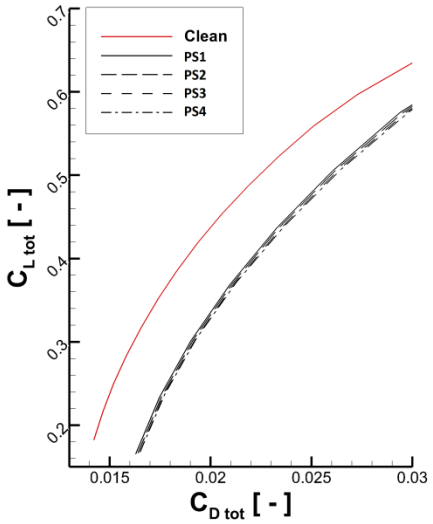

Figure 29 Lift-drag polar for baseline configuration in four engine power settings from PS1 to PS4; $Re = 45x10^6; M = 0.82$;

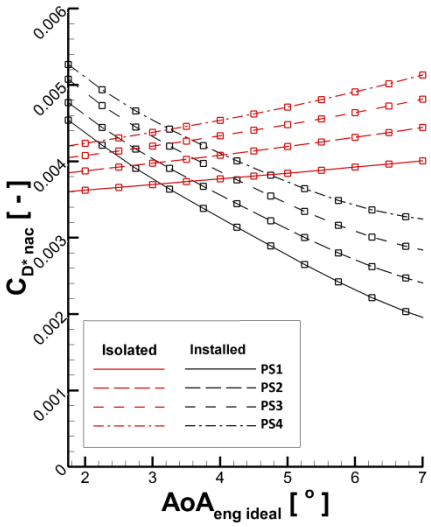

Figure 30 Modified engine drag ($C_{D^* nac}$) as function of engine ideal incidence ($AoA_{eng,ideal}$) for the baseline engine in isolation and under the wing in baseline position (C3) for a range of power settings from PS1 to PS4; $Re = 45x10^6; M = 0.82$;

The effect of the engine power setting, and associated MFCR, on the pressure distribution is localised to the fan cowl forebody (Figure 31). The reduction of power setting caused a reduction in intake MFCR and increased the spillage of the intake. As a result the peak suction at $\xi/L_{nac} = 0.05$ increases by approximately $\Delta C_p = -0.08$ every $\Delta MFCR = 0.05$. The effect of the wing on the central and aft section of the fancowl is broadly constant for all power settings and as a result almost no difference is observed beyond $\xi/L_{nac} > 0.3$. The aerodynamics on the suction side of the wing is indifferent to the changes of engine power setting from PS1 to PS4 (Figure 32) and a reduction in peak suction $\Delta C_p = +0.25$ is observed as compared with clean-wing configuration. However, a modest difference in the pressure distribution is observed on the lower side of the wing. The lowest power setting (PS4) has single suction peak $C_p = -0.17$ on the pressure side at $x/c = 0.55$. By increasing the power setting to PS1, the suction peak at $x/c = 0.55$ increases by $\Delta C_p = -0.03$, also a local pressure increases by $\Delta C_p = +0.03$ at $x/c = 0.3$.

As compared with the isolated engine, the installation of the engine under the wing affected the pressure distribution for the core cowl (Figure 33). The isolated engine at PS1 exhibits two distinct zones on the core cowl, one with expansion zone ($0.1 < \xi/L_{core} < 0.5$) with peak suction $C_p = -0.2$ at $\xi/L_{core} = 0.25$ and one compression zone ($0.5 < \xi/L_{core} < 0.1$) with peak pressure $C_p = +0.8$ at $\xi/L_{core} = 0.7$. As the engine was installed under the wing (Figure 33), the peak of the suction and peak of the pressure reduced by $\Delta C_p = +0.1$ at $\xi/L_{core} = 0.25$ and $\Delta C_p = -0.2$ at $\xi/L_{core} = 0.7$, as a result of the wing pressure-field. Moreover, the reduction in the power setting from PS1 to PS4 led to reduced FNPR (Table 2). As a result the flow physics changed and a constant constant value of $C_p = +0.25$ along the entire core cowl length (Figure 33) is reported. Furthermore, the effect of the wing pressure-field on the modified gross propulsive force (GPF^*) was assessed by considering the GPF^* for each power setting and non-dimensionalised by the GPF^*_{ref} for the respective power setting of an isolated engine (Table 2) at $AoA_{eng,ideal} = 0°$. The $AoA_{eng,ideal}$ was considered to make a consistent assessment for the isolated and the wing-installed engine and the effect of upwash was neglected, as a typical $AoA_{upwash} = +0.5°$ corresponds to a difference of only 0.02% of the GPF^* of an isolated engine. As for the isolated engine, the sensitivity of GPF^* to $AoA_{eng,ideal}$ depended on the engine power setting and was not monotonic. Overall, a broad trend for all power settings is defined as the GPF^* reduces by 0.5% over the entire range of incidence. As compared with the isolated

engine, the wing-installed engine has substantially different trend. A loss of GPF^* by 1.75% is observed for PS1 at $AoA_{eng,ideal} = 1.75°$ and as the $AoA_{eng,ideal}$ increases, a benefit of +1% in GPF^* is observed at $AoA_{eng,ideal} = 7°$. As the engine power setting of an installed engine reduces from PS1 to PS4, a non-monotonic performance is noted.

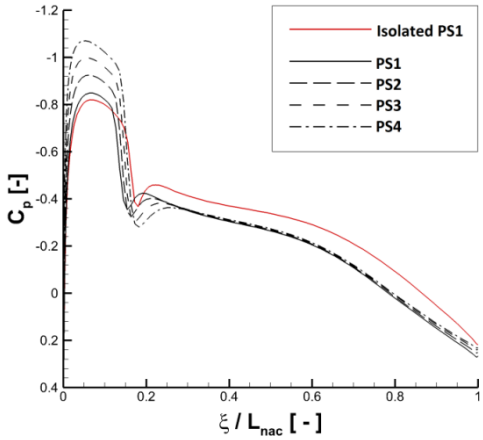

Figure 31 Pressure distribution (C_p) on the top line of the fan cowl for baseline configuration (C3) in four engine power settings represented by MFCR at $AoA_{eng,ideal} = 4.25°$ ($AoA_{A/C} = 2.5°$), compared with isolated engine at $AoA_{eng,ideal} = 4.25°$; $Re = 45x10^6; M = 0.82$;

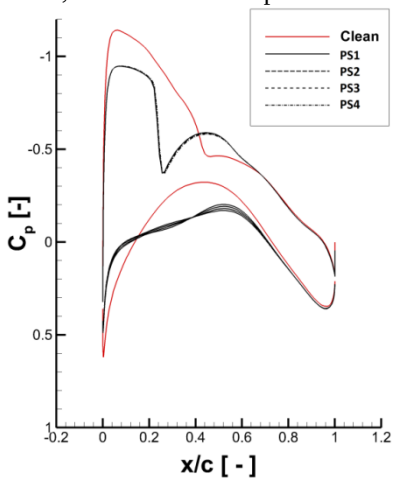

Figure 32 Pressure distribution at wing cross-section at engine installation plane (y/b = 0.283) at $AoA_{A/C} = 2.5°$ for baseline configuration (C3) in four engine power settings represented by MFCR, compared with clean-wing configuration ; $Re = 45x10^6; M = 0.82; AoA_{A/C} = 2.5°$

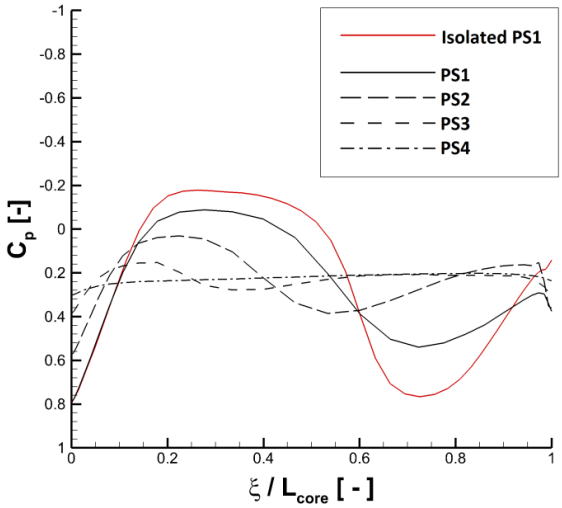

Figure 33 Pressure distribution (C_p) on the top line of the core cowl for baseline configuration (C3) in four engine power settings at $AoA_{eng,ideal} = 4.25°$ ($AoA_{eng} = 2.5°$), compared with isolated engine at $AoA_{eng,ideal} = 4.25°$; $Re = 45x10^6; M = 0.82$;

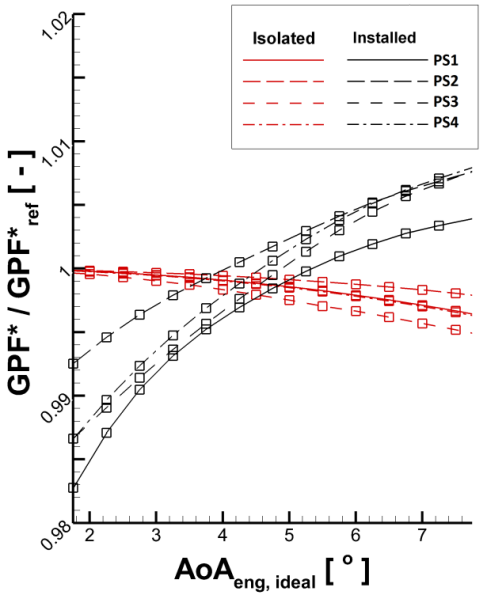

Figure 34 Non-dimensionalised modified gross propulsive force (GPF^*/GPF^*_{ref}) for baseline configuration (C3) in four engine power settings compared with isolated engine; $Re = 45x10^6; M = 0.82$

IV. Conclusions

The effects of engine installation for a typical wide body aircraft with 250-300 passenger seats were assessed with use of Computational Fluid Dynamics. For the baseline configuration at typical cruise lift coefficient $C_{L\,tot} = 0.5$, the installation of an engine caused a computed drag penalty of approximately 35 dc as compared with the clean-wing configuration. This installation penalty of 35 dc corresponds to approximately 14% of the overall aircraft drag in cruise. The installation drag is sensitive to aircraft incidence, engine position and power setting. The computed sensitivity to engine position at typical cruise lift coefficient $C_{L\,tot} = 0.5$ was 9dc over the entire range of positions considered here and it corresponds to 3.5% of the overall aircraft drag. At the datum engine position, the sensitivity of the installation drag to power setting is 3 dc over the range of investigated power settings, which correspond to a range of mass flow capture ratio (MFCR) from 0.6 to 0.75 and fan nozzle pressure ratios (FNPR) from 2.12 to 2.71. Overall the installation effects are affected by interactions between the wing pressure-field and the engine. The wing pressure-field exerts a pressure force on the aft of the fan cowl as well as on the exhaust system of the engine. At cruise conditions the pressure force exerted on the fan cowl afterbody reduces the nacelle drag by approximately 20% (10dc) as compared with an isolated engine. The effect on the viscous drag was negligible. As the engine exhaust system is exposed to the wing pressure-field, the engine gross propulsive force (GPF_ξ^*) was also affected by the engine installation. Under cruise conditions the changes in GPF_ξ^* varied from a -0.1% penalty to a 0.6% benefit depending on the engine installation position relative to the wing.

References

1. Advisory Group for Aerospace Research and Development (AGARD), "Special course on Subsonic/Transonic Aerodynamic Interference for Aircraft", AGARD Report No. 712, 1983. Tech. rep. AGARD-R-712
2. Lee, E. E., Pendergraft Jr, O. C., "*Installation effects of long-duct pylon-mounted nacelles on a twin-jet transport model with swept supercritical wing*", NASA. 1985. Tech. rep.
3. Carlson, J. R., Compton, W. B., "*An experimental investigation of Nacelle-pylon installation on an unswept wing at susbonic and transonic speeds*", NASA. 1984. Tech. rep.
4. Hoheisel, H., "Aerodynamic aspects of engine-aircraft integration of transport aircraft",*Aerospace Science and Technology*,Vol. 1, No 7, 1997, pp. 475-487.
5. Brodersen, O. "Computation of Engine-Airframe Installation Drag" *MEGAFLOW - Numerical Flow Simulation for Aircraft Design*, edited by Kroll, N., Fassbender, J.,Vol. 89, Springer, Berlin, 2005. pp. 151-161.
6. Rossow, C-C., Nashville, T. N., "Investigations of Propulsion Integration Interference Effects on a Transport Aircraft Configuration",*AIAA/SAE/ASME/ASEE 28th Joint Propulsion Conference and Exhibit*.,6-8 July 1992. Vols. AIAA 92-3097.
7. Geyr, H. Frhr. Von, Rossow, C. C., "*A correct thrust detemination method for turbine powered simulatiors in wind tunnel testing*",41st AIAA/ASME/SAE/ASEE Joint Propulsion Conference & Exhibit,2005, pp. 1-12, AIAA Paper No. 2005-3707
8. Oliveira, G.L., Trapp, L.G., Puppin-Macedo, A., "Integration Methodology for Regional Jet Aircraft with Underwing Engines", *41st Aerospace Sciences Meeting and Exhibit*, 6-9 January, Reno, Nevada, United States, AIAA Paper No. 2003-934
9. Frink N. T., 2nd AIAA CFD Drag Prediction Workshop. [Online] AIAA, June 21-22, 2003. [accessed 10.04.2015] http://aaac.larc.nasa.gov/tsab/cfdlarc/aiaa-dpw/Workshop2/workshop2.html
10. Vassberg, J. C., et al. " Development of a Common Research Model for Applied CFD Validation Studies", AIAA. 2008. AIAA Paper No. 2008-6919.
11. Rivers, M. B., Dittberner, A., "Experimental investigations of the NASA Common Research Model in the NASA Langley National Transonic Facility and NASA Ames 11-Ft transonic wind tunnel (invited)", *49th AIAA aerospace sciences meeting including the new horizons forum and aerospace exposition*, Orlando, Florida, US 2010, AIAA Paper No. 2011-1126.
12. Rivers, M. B., "Experimental investigation of the NASA Common Research Model (Invited)", *28th AIAA Applied Aerodynamics Conference*, Chicago, Illinios, US, 2010, AIAA Paper No. 2010-4218
13. Macmillan, W. L., Development of a Module Type Computer Program for the Calculation of Gas Turbine Off Design Performance, Ph.D. thesis, Departmentof Power and Propulsion, Cranfield University, 1974.
14. Kulfan, B., Bussoletti, J., *""Fundamental" Parameteric Geometry Representations for Aircraft Component Shapes*" in 11th AIAA/ISSMO Multidisciplinary Analysis Optimization Conference, American Institute of Aeronautics and Astronautics, AIAA Paper No. 2006-6948.

15. Ceze, M., Hayashi, M., Volpe, E., "*A Study of the CST Parameterization Characteristics*," in 27th AIAA Applied Aerodynamics Conference, American Institute of Aeronautics and Astronautics, 2009.
16. Frink N. T., 4th AIAA CFD Drag Prediction Workshop. [Online] AIAA, June 20, 2009. [accessed: 10.04.2015.] http://aaac.larc.nasa.gov/tsab/cfdlarc/aiaa-dpw/Workshop4/workshop4.html.
17. Tinoco, E. N., Levy, D., Brodersen, O., "DPW-IV Summary of Participants Data", *AIAA 4th CFD Drag Prediction Workshop*, San Antonio, Texas, 2009.
18. Menter, F. R., "Two-equation eddy-viscosity turbulence models for engineering applications", AIAA Journal, Vol. 32, No. 8, 1994, , pp. 1598-1605.
19. Christie, R., Ramirez, S. and MacManus, D. G., "Aero-engine installation modelling and the impact on overall flight performance", In: *Advanced Aero Concepts, Design and Operations Conference*, 27 June 2014, Bristol, United Kingdom.
20. Stańkowski, T.P., MacManus, D.G., "Engine installation module development for an aircraft mission analysis framework" , In: *Advanced Aero Concepts, Design and Operations Conference*, 27 June 2014, Bristol, United Kingdom.
21. Stańkowski, T.P., MacManus, D.G., "Aerodynamics of aero-engine installation", IMECHE Part G (to be published)
22. Roache, P.J., "Perspective: a method for uniform reporting of grid refinement studies"*Journal of Fluids Engineering*, Vol. 116, No. 3, 1994, pp. 405-413.
23. Kwasniewski, L., "Application of grid convergence index in FE computation", *Bulletin of the Polish Academy of Sciences, Technical Sciences*, Vol. 61, No. 1, 2013, pp. 123-128.
24. Voulgaris, I., Civil Aircraft Nacelle and Afterbody Aerodynamics, Master's thesis, Cranfield University, Bedfordshire, UK, August 2014.
25. Kiock, R. and Baumert, W., "A Selection of Experimental Test Cases for the Validation of CFD codes, Volume II," Advisory Group for Aerospace Research and Development, AOARD-AR-303 Vol. 2, 7 Rue Ancelle, 92200 Neuilly-sur-Seine, France, August 1994.
26. Baumert,W., Binder, B., and Stager,W., "Engine Simulator Tests: Comparison of Calibration and Wind Tunnel Results," Advisory Group for Aerospace Research and Development, AGARD-CP 429, 7 Rue Ancelle, 92200, Neuilly-sur-Seine, France, 1987.
27. ESDU,"Introduction to the Measurement of Thrust in Flight (Air Breathing Ducted Flow Engines)", ESDU. 1981. Tech. rep. ESDU-69006
28. Ministry-Industry Drag Analysis Panel (MIDAP) Study Group, "Guide to in-flight thrust measurement of turbojets and fan engines", AGARDograph No. 237 AGARD. 1979.

Aerodynamics of aero-engine installation

Stankowski, Tomasz P.

2016-01-02

Stankowski TP, MacManus DG, Sheaf CT & Grech N. Aerodynamics of aero-engine installation.
In: 54th AIAA Aerospace Sciences Meeting, San Diego, 4-8 January 2016, Paper number AIAA 2016-0764
https://doi.org/10.2514/6.2016-0764